DEUTSCHES ELEKTRONEN-SYNCHROTRON DESY

DESY SR-81/05
September 1981



# ATOMIC SPECTROSCOPY WITH SYNCHROTRON RADIATION

by

Bernd F. Sonntag
*II. Institut für Experimentalphysik der Universität Hamburg*

NOTKESTRASSE 85 · 2 HAMBURG 52

To be sure that your preprints are promptly included in the
HIGH ENERGY PHYSICS INDEX ,
send them to the following address ( if possible by air mail ) :

DESY
Bibliothek
Notkestrasse 85
2 Hamburg 52
Germany

DESY SR-81/05
September 1981

# ATOMIC SPECTROSCOPY WITH SYNCHROTRON RADIATION

Bernd F. Sonntag

II. Institut für Experimentalphysik, Universität Hamburg, 2000 Hamburg, Federal Republic of Germany

Abstract - The continuous spectrum extending from the infrared to the x-ray region, the high intensity, the time structure and the high degree of polarization of synchrotron radiation makes electron storage ring sources unique for atomic spectroscopy. Vacuum ultraviolet photons can excite loosely bound electrons to high energy continuum states and deeply bound core electrons to bound states below and continuum states above the ionization limit. The interaction between the different excitation channels strongly influences the spectra. Many-electron correlations often result in a complete break-down of the independent particle approximation. The impact of synchrotron radiation on atomic spectroscopy will be showcased by reviewing the most important recent experimental results together with the pertinent theoretical models.

## PROPERTIES OF SYNCHROTRON RADIATION

Synchrotron radiation is emitted by relativistic electrons circulating in electron synchrotrons or electron storage rings. The following outstanding properties make synchrotron radiation one of the most useful sources for spectroscopy (Ref.1 & 2):

1. continuous spectrum from the infrared to the x-ray region
2. collimation of the radiation in a narrow cone around the instantaneous direction of flight of the electrons
3. linear polarization in the plane of the electron orbit; circular polarization above and below the orbit
4. time structure with pulse lengths down to 100 ps
5. absolute calculability of the properties of the source
6. cleanliness of the source, since emission takes place in ultra high vacuum.

As an example, the spectral distribution of the intensity emitted by the electron storage ring DORIS is presented in Fig.1.

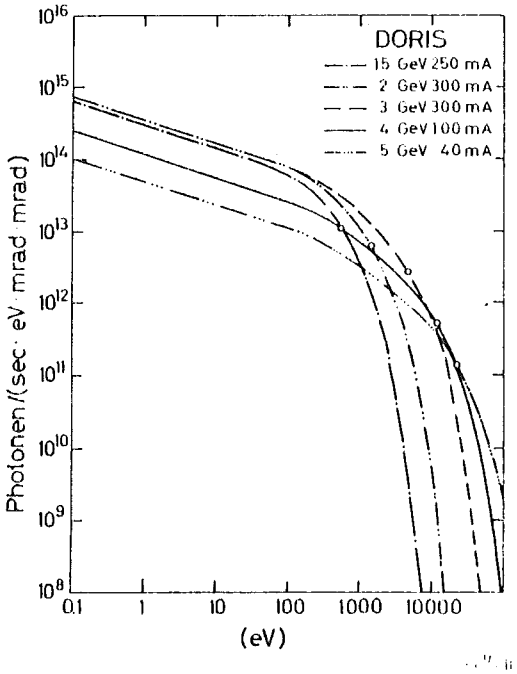


Fig. 1 Spectral distribution of intensity in an aperture 1 mrad wide and 1 mrad high centered at a tangential direction.

### Central potential model

The most characteristic features of the vacuum-ultraviolet (VUV; 10 eV < $\hbar\omega$ < 1000 eV) spectra of atoms can be described qualitatively within the framework of a central field model based on a realistic potential (Ref. 3&4). The central potential most widely used with reasonable success is the Hartree Slater (HS) potential calculated, for example, by Herman and Skillmann (5). The non-Coulomb

Proceedings of the 9th International Conference on Atomic Spectroscopy/ XXII Colloquium Spectroscopicum Internationale, Tokyo (Japan), 4-8 Sept. 1981, published by Pergamon Press.

character of the HS-potential for intermediate radii is crucial for the characteristic features of the VUV spectra. Combining the HS-potential U(r) and the centrifugal term $\frac{\ell(\ell+1)}{2r^2}$ results in an effective potential

$$V_{eff} = U(r) + \frac{\ell(\ell+1)}{2r^2}$$

The interplay between the attractive U(r) and the repulsive centrifugal term results in single valley, double valley and repulsive potentials. The double valley potential seen by the Xe f-electrons is depicted in Fig. 2. A pronounced positive barrier separates the inner and the outer valley. The radial wave functions $P_{n,\ell}(r)$ obey the Schrödinger equation

$$\left(-\frac{d}{dr^2} + V_{eff}(r)\right) P_{n,\ell}(r) = \varepsilon_{n,\ell} \; P_{n,\ell}(r)$$

For Xe the radial wave function of the bound 4d state and several f-symmetric continuum states are included in Fig. 2. The photoionization cross-section is determined by the matrix element $R_{\ell\pm1}$ which in the dipole-length form is given by

$$R_{\ell\pm1} = \int_0^\infty P_{n,\ell}(r)\; r\; P_{\varepsilon,\ell}(r)\; dr$$

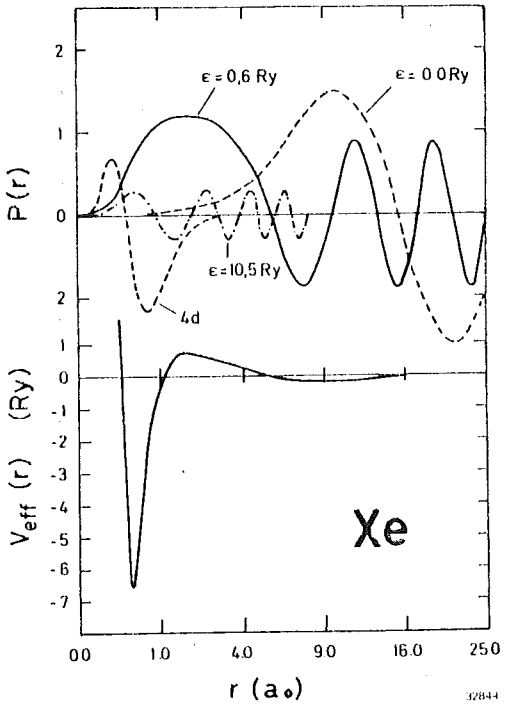


Fig. 2 bottom: effective potential $V_{eff}(r)$ for f-electrons of Xe.
top: Xe - 4d $P_{4,d}(r)$ and f continuum $P_{\varepsilon,f}(r)$ radial wavefunctions for different kinetic energies $\varepsilon$.

The Xe 4d photoionization is dominated by transitions into f-symmetric continuum states. The characteristic features of the Xe 4d spectrum shown in Fig. 3 can be directly read off from Fig. 2. At threshold, i.e. for low kinetic energies $\varepsilon$ of the outgoing photoelectron, the final state radial wave function is centered in the outer potential valley and hardly overlaps with the 4d wave function.

This explains the delayed onset of absorption at threshold. Towards higher energies the final state wave function penetrates closer to the nucleus, resulting in a larger overlap and a higher transition probability. At $\varepsilon$ = 0.6 Ry the absolute value of the matrix element peaks, giving rise to the pronounced maximum in the experimental spectrum. Note that due to the different sign of the 4d and $\varepsilon$f wave functions in the region of overlap, the matrix element is negative. For still higher energies the first node of the f-symmetric wave function moves into the inner valley. At $\varepsilon$ = 10.5 Ry the matrix element is zero due to the cancellation of the positive and negative contributions. The zero of the matrix element explains the Cooper minimum found at 150 eV in the experimental spectrum.

Photoionization of closed shell atoms

From Fig. 3 it is obvious that the results of central-potential calculations can only be considered as a guideline. The cross-sections obtained by Hartree-Fock calculations are in far better agreement with the experimental cross-sections than those obtained within the central potential model. In case of the HF calculations the radial wave function of the continuum electron ionized from the n$\ell$-th subshell is obtained by solving the HF equation in the frozen core of the positive ion with an n$\ell$-hole (Ref. 9). This approach is equivalent to taking intrachannel interactions into account (Ref.8). In comparison with experiment the intrachannel interaction over-corrects the central potential calculation. These discrepancies have been resolved by the random phase approximation with exchange (RPAE) (Ref. 10). In RPAE the electric dipole matrix elements are calculated directly treating initial and final state correlations simultaneously. Compared to the HF calculation, the most important improvement results from the inclusion of virtual double-excitations in the ground and ionic states. For closed shell atoms the RPAE cross-sections agree with the experimental cross-sections within less than 10% in most cases (Ref.4&11). Similar agreement between theory

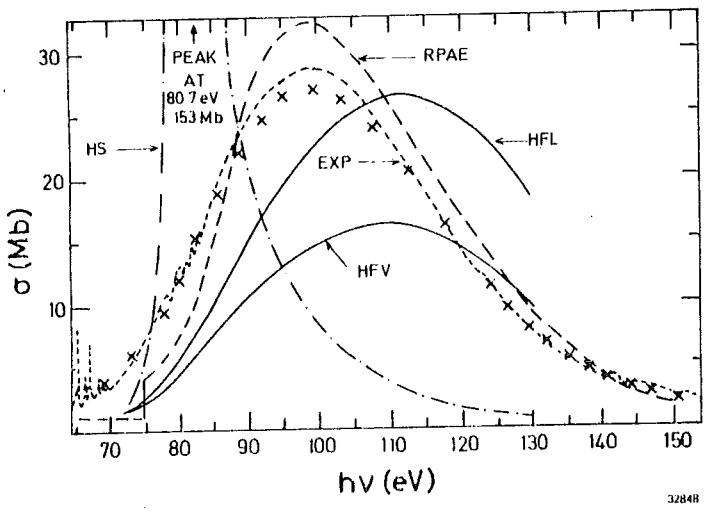


Fig. 3

Photoionization cross-section for the 4d subshell of Xe. Experimental data from Haensel et al. (Ref. 6) (- - - -) and West and Morton (Ref. 7) (x x x). Theoretical results: Herman-Skillman central potential calculation (-·-); Hartree-Fock length (HFL) and velocity (HFV) calculations (Ref. 8&9), calculations within the random phase approximation (including exchange (RPAE) (Ref. 10).

and experiment has been achieved e.g. by multiconfiguration Hartree-Fock (Ref. 12), transition matrix (Ref. 13), many-body perturbation (Ref. 14, 15), R-matrix (Ref. 15) and density functional (Ref. 17) calculations. For a discussion of the different theoretical approaches, their successes and failures, the reader is referred to the excellent reviews by Starace (Ref. 4, 18).

Photoionisation of open shell atoms

For open shell atoms our understanding of the VUV photoionisation is far less satisfactory (Ref. 4, 11, 18, 19). In most cases the preparation of free open shell atoms requires high temperatures which in combination with the restrictions imposed by VUV optics amounts to non-trivial experimental difficulties. The great number of channels contributing to photoionization causes headaches to the theorists. The experimental set-up used at the Electron Synchrotron DESY for the determination of the absorption of high temperature metal vapors is presented in Fig. 4 (Ref. 20).

Fig. 4

Experimental set-up at DESY for the determination of high temperature vapor absorption spectra.

Sl = incoming synchrotron radiation
S = sample pipe,
H = Ta heating pipe
W, M, V = radiation shields, T = vacuum tank, Sv = shutter,
F = thin film window

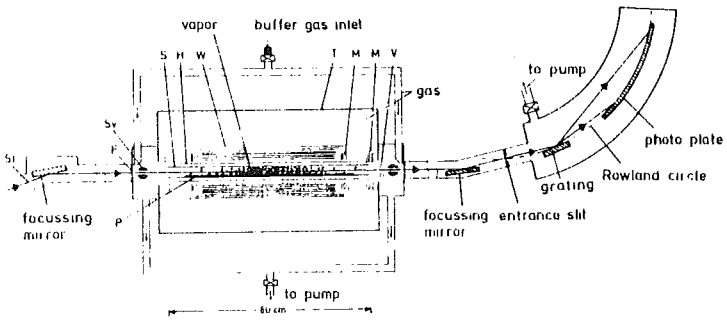


The atomic metals were maintained inside a resistance-heated tubular furnace mounted in front of a 2 m grazing incidence Rowland-type spectrograph. The term dependent break down of the subshell concept for the 3p-excitations of atomic 3d metals clearly manifests itself in the spectrum of Mn presented in Fig. 5. The weak, sharp lines at the 3p threshold are due to $3p^6\ 3d^5\ 4s^2\ {}^6S \rightarrow 3p^5\ 3d^6\ {}^6F$ (lines 1-3), ${}^6D$ (line 4) ${}^4P$ (lines 5,6) transitions. The dominant asymmetric absorption band is assigned to the LS allowed $3p^6\ 3d^5\ 4s^2\ {}^6S \rightarrow 3p^5\ 3d^5\ 4s^2\ {}^6P$ transitions. These transitions are strongly coupled to $3p^6\ 3d^5\ 4s^2\ {}^6S \rightarrow 3p^6\ 3d^4\ 4s^2\ \varepsilon f\ {}^6P$ transitions via the Super-Coster-Kronig decay $3p^5\ 3d^6\ 4s^2\ {}^6P \rightarrow 3p^6\ 3d^4\ \varepsilon f\ {}^6P$. The interference between the two channels gives rise to the Fano type line shape (Ref.3, 24)

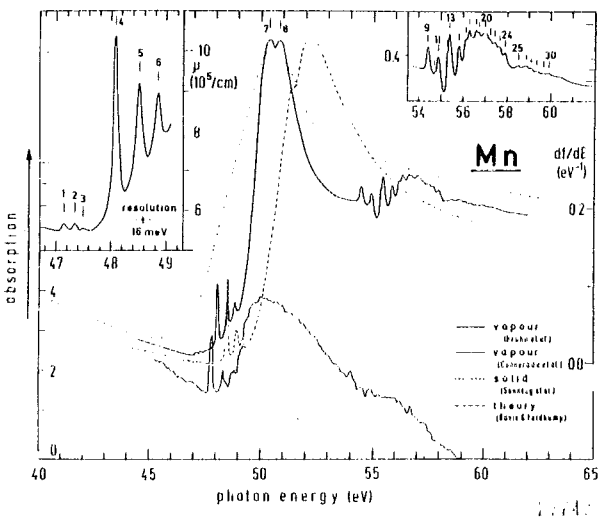


Fig. 5

3p-absorption of atomic and metallic (Ref. 22) Mn. The lower solid line gives the densitometer trace reported by Connerade et al. (Ref. 23). The absolute absorption coefficient refers to the spectrum of metallic Mn. The oscillator strength df/dE for atomic Mn calculated by Davis and Feldkamp (Ref. 24) is included.

$$\sigma(E) = \sigma_c(E)\,\frac{\left(q + \frac{E-E_r}{\Gamma}\right)^2}{1+\left(\frac{E-E_r}{\Gamma}\right)^2}$$

where $\sigma_c(E)$ gives the 3d → f continuum cross-section in the absence of the interaction with the 3p → 3d transition, q is the asymmetry parameter, $E_r$ the energy of the resonance and $\Gamma$ the half width. This interpretation of Mn 3p spectrum has been corroborated by recent photoemission measurements on Mn atoms (Ref. 25). Fig. 6 shows the 3p absorption spectrum of atomic Cu (Ref. 20). Since the 3d shell is filled in Cu, there is no strong maximum at threshold. The weak maxima are ascribed to 3p → ns, nd transitions. Davis and Feldkamp (Ref. 26) have shown that the dip in absorption above the 3p → 4s peaks can be explained by the interference of 3p → nd, fd and 3d → εf channels. The interaction between the 3p and 3d excitations also manifests itself in the minimum of the 3d cross-section for metallic Cu (Ref.27).

Resonant photoemission

The analysis of the energy and angular distribution of the outgoing photoelectron allows by far more stringent tests of theoretical approaches than those based on absorption spectra. In Fig. 7 an experimental set-up for energy and angular resolved photoemission, in atmospheric gases, operated with great success at the NBS is shown (Ref. 28&29).

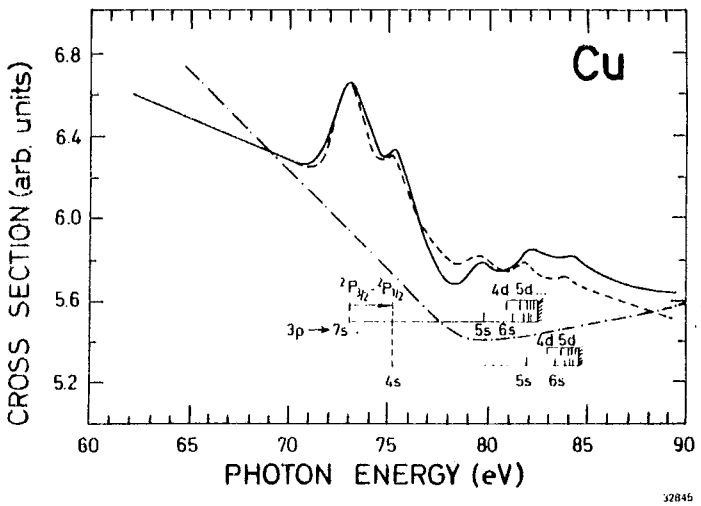


Fig. 6

Absorption of atomic Cu at the 3p threshold, experiment (——) (Ref. 20), theory (- - -) (Ref. 26). $\sigma_{3d}$ for metallic Cu (-.-.-) (Ref. 27).

Fig. 7

Angle resolved photoelectron spectrometer coupled to a high throughput 2 m normal incidence monochromator in operation at SURF-II (Ref. 28 & 29).

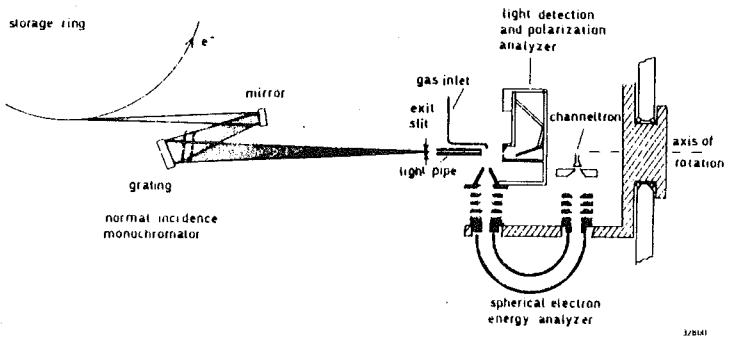


In case of photoemission from atomic metals, the requirement to combine a high temperature intense vapor source with an electron spectrometer adds to the experimental difficulties. An experimental arrangement described by Shannon and Codling (Ref. 30) is presented in Fig. 8.

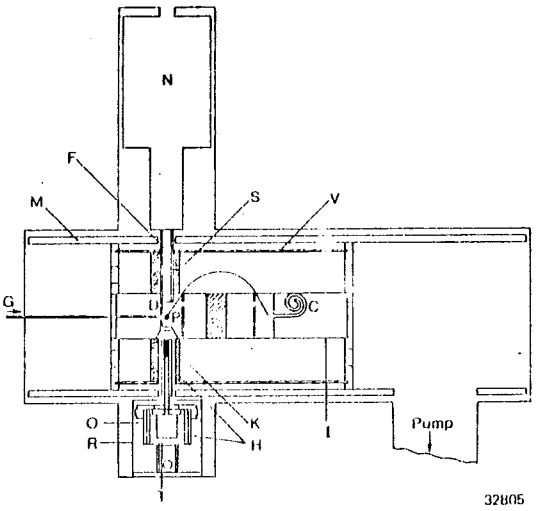


Fig. 8

Cylindrical electron energy analyser with oven.
N = liquid $N_2$ reservoir
F = cold finger
M = mu metal
D = cold shield
G = calibration gas inlet
P = photon beam
O = oven
R = radiation shields
T = thermocouple
H = heating coils
K = collimator
I = inner cylinder
V = outer cylinder
C = channeltron (Ref.30)

Most of the VUV experiments reported so far have been restricted to systems providing sufficient vapor-pressure at temperatures below $1000^{\circ}$ C. Recently Chandesris et al. (Ref. 31) succeeded in determining the photoemission of atomic Cu for photon energies between 70 eV and 80 eV. The experimental spectrum is given in Fig. 9. The main line corresponds to the $3d^9\ 4s$ configuration of $Cu^+$. The five weaker satellite structures have been ascribed to the $3d^8\ 4s$ ($^1S$, $^1G$, $^3P$, $^1D$, $^3F$) multiplet (Ref. 31). The most interesting result is the resonant enhancement of the $^1G$ and $^3F$ lines when tuning the photon energy through the $3p^6\ 3d^{10}\ 4s \rightarrow 3p^5\ 3d^{10}\ 4s^2$ transition of Cu (see Fig. 6). The variation of the intensity of the $^1G$ and $^3F$ satellite lines between 70 eV and 78 eV is shown in Fig. 10.

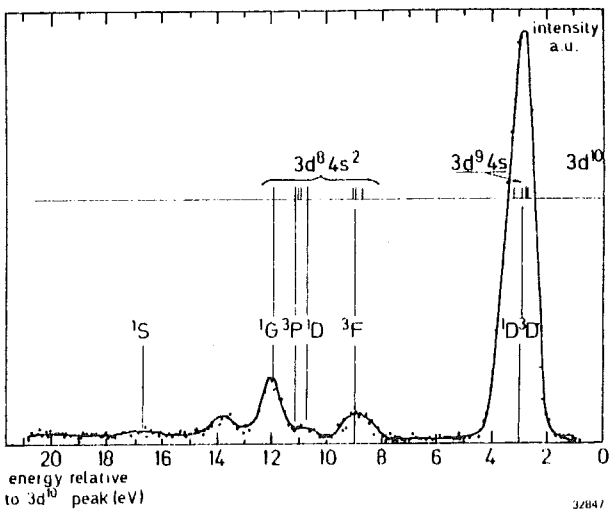


Fig. 9

Photoelectron spectrum of atomic Cu.

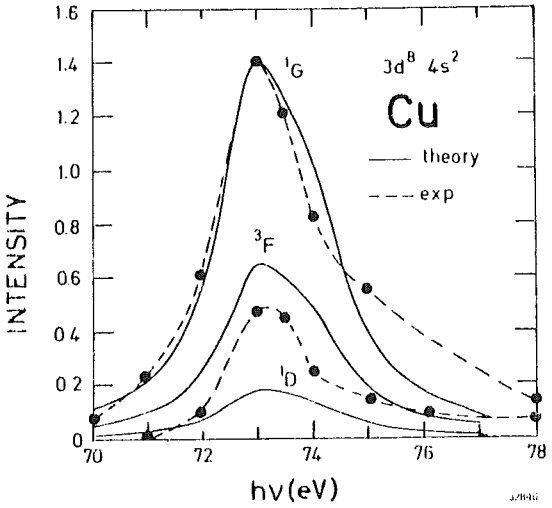


Fig. 10

Intensity of the $^1G$, $^3F$ and $^1D$ satellites as a function of photon energy.

Experiment (-·-·) (Ref. 31); Theory (—) (Ref. 26).

The resonant enhancement of the two electron satellites is due to the super-Coster-Kronig decay of the $3p^3\ 3d^{10}\ 4s^2\ ^2P_{\frac{1}{2},\frac{3}{2}}$ state, primarily in the $^1G$ multiplet and with lesser amounts in $^3F$ and $^1D$ of $Cu^+\ 3d^8\ 4s^2$. The interference between the

$$3p^6\ 3d^{10}\ 4s \rightarrow 3p^5\ 3d^{10}\ 4s^2$$

and the two-electron excitation $3p^6\ 3d^{10}\ 4s \rightarrow 3p^6\ 3d^8\ 4s^2\ \varepsilon f$

via the super Coster-Kronig decay $3p^5\ 3d^{10}\ 4s^2 \rightarrow 3p^6\ 3d^8\ 4s^2\ \varepsilon f$

is negligible, because of the small oscillator strength of the two-electron excitation. This explains the symmetric Lorentzian type line shape. Note that in the calculations (Ref. 26) the spin orbit splitting of the Cu 3p level has been taken into account. Because of the small probability for the Auger decay $3p^5\ 3d^{10}\ 4s^2 \rightarrow 3p^6\ 3d^9\ 4s\ \varepsilon f$,

the main $3d^9\ 4s$ line is hardly affected, when tuning the photon energy through the $3p \rightarrow 4s$ resonance.

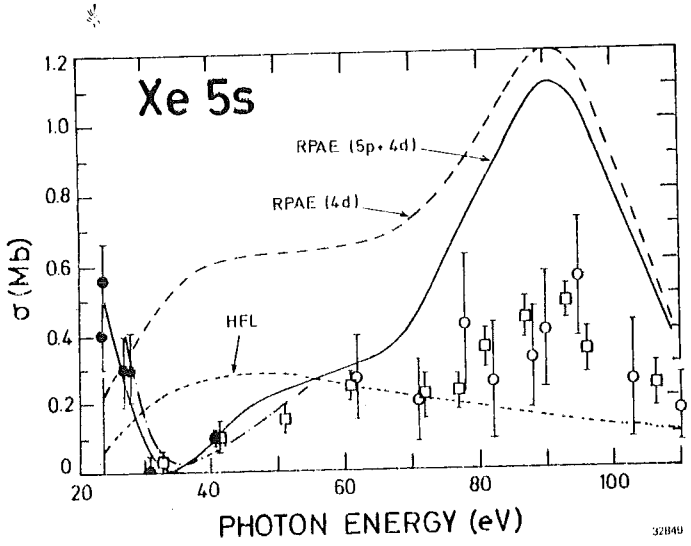


Fig. 11

Xe 5s subshell photoionization cross-section. Experiment (●) (Ref. 32) (○) (Ref. 33); (□) (Ref. 34) theory, RPAE and HFL (Ref. 10); RRPA (-·-·-) (Ref. 35).

Interchannel interaction

The striking effects of interchannel interaction are well showcased for the photoionization cross-sections of the outer s-subshells of the rare gas atoms. The Xe 5s subshell cross-section is presented in Fig. 11. In contrast to the Hartree-Fock length (HFL) result, the experimental curve shows a minimum at 34 eV and a maximum at ∿ 90 eV (Ref. 32, 33, 34). The minimum mirrors the Cooper minimum in the 5p → εd channel, the maximum the delayed maximum in the 4d →εf channel. Including the coupling of the 5s, 5p and 4d channels, the main features of the experimental spectrum are well reproduced by the RPAE calculations by Amusia and Cherepkov (Ref. 10). The calculations by Johnson and Cheng (Ref. 35) using the relativistic randomphase approximation RRPA reproduced the experimental results in the region of the minimum above threshold very well. Relativistic effects are responsible for the nonzero of the cross-section at the minimum.

Branching ratio

The branching ratio, i.e. the ratio of the photoemission intensity from two subshells split by the spin-orbit interaction, often considerably deviates from the statistical ratio given by the occupation numbers of the subshells. Cross-sections varying with photon energy in combination with the different kinetic energies of the outgoing electrons contribute to these deviations (Ref. 36). But this effect by no means can explain the experimental results. Relativistic effects and interchannel interaction play a very important role. This is clearly demonstrated by the $^2P_{3/2}$ : $^2P_{1/2}$ branching ratio for the Xe 5p photoemission presented in Fig. 12. Only the RRPA calculations (Ref. 35) including the coupling of the 5s, 5p and 4d channels are able to reproduce the experimental results.

Fig. 12

$^2P_{3/2}$ : $^2P_{1/2}$ branching ratio for Xe 5p.
Experiment: (•••) (Ref. 37); (⧳) (Ref. 38);
Theory:
(—) (Ref. 35);
(- - -) (Ref. 39);
(-•-) and (—••—) (Ref. 38).

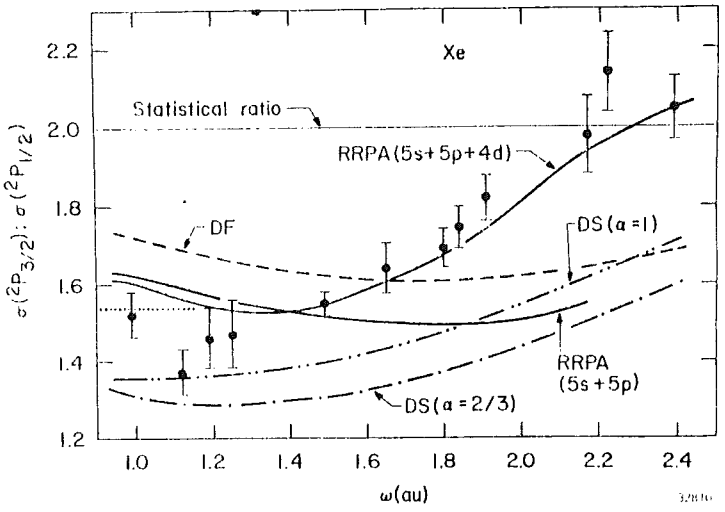

Angular resolved photoemission

Angular and energy resolved photoemission measurements form a stringent test for theoretical models, because they yield information on the absolute value and the sign of the matrix element and on the phase of the final state wavefunction (Ref. 4). In LS coupling for closed shell atoms the Cooper Zare model (Ref. 40) holds. The differential photoionisation cross-section for linearly polarized incoming light, in dipole approximation, is given by

$$\frac{d\,ij\,(\varepsilon)}{d\Omega} = \frac{\sigma ij\,(\varepsilon)}{4\pi}\left[1 + \beta ij\,(\varepsilon)\,\frac{1}{2}\,(3\cos^2\psi - 1)\right]$$

where i, j stand for the quantum numbers of the initial, final state respectively, $\sigma ij\,(\varepsilon)$ is the partial photoionisation cross-section, $\psi$ is the angle between the direction of the outgoing photoelectron and the electric vector of the light. The asymmetry parameter $\beta ij\,(\varepsilon)$ characterizing the angular distribution of the photoelectrons is given by

$$\beta_{n,\ell} = \frac{\ell(\ell-1)R^2_{\ell-1}(\varepsilon) + (\ell+1)(\ell+2)R^2_{\ell+1}(\varepsilon) - 6\ell(\ell+1)R_{\ell-1}(\varepsilon)R_{\ell+1}(\varepsilon)\cos\left[\delta_{\ell+1}(\varepsilon) - \delta_{\ell-1}(\varepsilon)\right]}{(2\ell+1)\left[\ell R^2_{\ell-1}(\varepsilon) + (\ell+1)\,R^2_{\ell+1}(\varepsilon)\right]}$$

where $\delta_\ell$ gives the partial wave phase shift. The second term depends on the matrix elements and the phases of the continuum wave functions. This term represents the interference between the $\ell \rightarrow \ell+1$ and $\ell \rightarrow \ell-1$ transitions. Fig. 13 shows the experimental (Ref. 41, 42) and theoretical (Ref. 9, 43) $\beta$ values for the Ar 3p excitation.

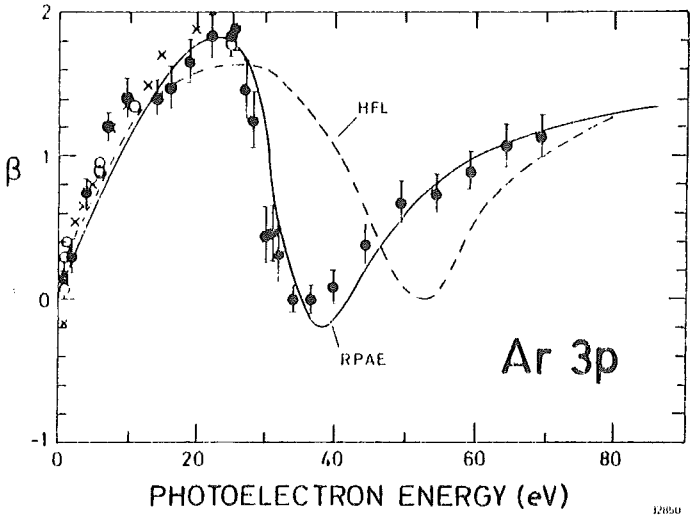


Fig. 13

Asymmetry parameter for the 3p shell of Ar. Experiment: (●,○)(Ref. 41)); (x) (Ref.42) Theory: HFL (Ref. 9); RPAE (Ref. 43).

The rapid increase of $\beta$ within the first eV above threshold is due to the variation of the phase shift. The Cooper minimum in the $3p \rightarrow \varepsilon d$ channel causes the minimum in the $\beta$ spectrum at $\sim$ 35 eV. The HFL results (Ref. 43) based on the Cooper Zare model show the characteristic features of the spectrum, though the position of the minimum is at too high energies. Good agreement with the experimental results has been achieved by RPAE calculations (Ref. 43) taking intershell correlations into account. Recent RRPA (Ref. 35) and R-matrix (Ref. 44) calculations give results in close agreement with the RPAE predictions.

Spin polarisation of photoelectrons

For a complete characterization of a photoionisation process, i.e. for the determination of all matrix elements and phase differences of continuum wave functions involved, the measurement of the total and partial cross-sections and the angular distribution of photoelectrons is not sufficient in general. Additional information can be obtained by the determination of the spin polarisation of the outgoing photoelectrons. Making use of the circular polarisation of the synchrotron radiation above and below the electron orbit, Heinzmann and coworkers (Ref. 45, 46, 47) succeeded in determining the total spin polarisation of the Ar 3p, Kr 4p, Xe 5p photoelectrons in the wavelength range 45 to 100 nm. A schematic diagram of the experimental set-up is shown in Fig. 14. A 10 m plane grating normal-incidence monochromator was used.

Fig. 14

Experimental set-up for the determination of the total spin polarisation (from Ref. 46).

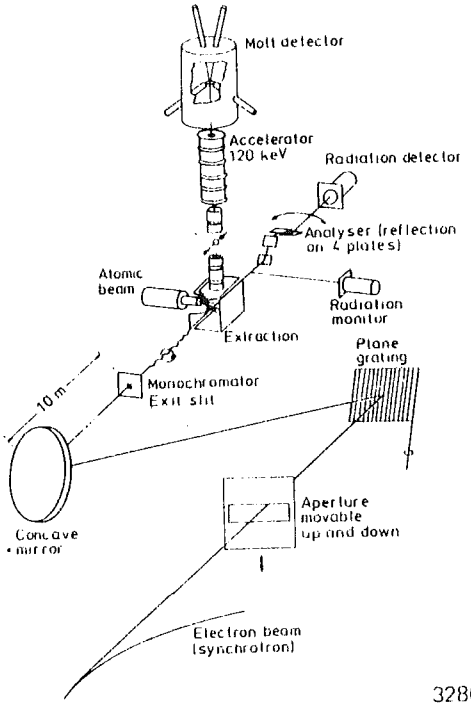


The concave mirror formed an image of the electron beam at the exit slit of the monochromator. Left or right circular polarisation was selected by the aperture which was movable perpendicular to the plane of the electron orbit. The degree of polarisation of the radiation was determined with a four mirror analyser.

The photoelectrons created at the crossing of the photon beam and the atomic beam were extracted by an electric field, focused by electron optical components and accelerated to 120 keV for polarisation analysis in a Mott detector. The experimental results for atomic Xe are shown in Fig. 15.

The prominent resonance structures above the $^2P_{3/2}$ ionisation limit (102,2 nm) are due to the autoionising $5p^6 \rightarrow 5p^5\ (^2P_{1/2})nd$ (broad structures) $5p^6 \rightarrow 5p^5\ (^2P_{1/2})ns$ (sharp lines) transitions (see e.g. Ref. 11). The interaction between the discrete and continuum states gives rise to the asymmetric Fano type line shapes (Ref. 3). The resonance structure is also shown by the photoelectron spin polarisation. The results of the multichannel quantum defect theory (MQDT) calculations (Ref. 48) by Lee are well reproducing the characteristic features of the experimental results. An even better agreement between theory and experiment has been achieved by Johnson et al. (Ref. 49) calculating the MQDT parameters within the relativistic random phase approximation (RRPA).

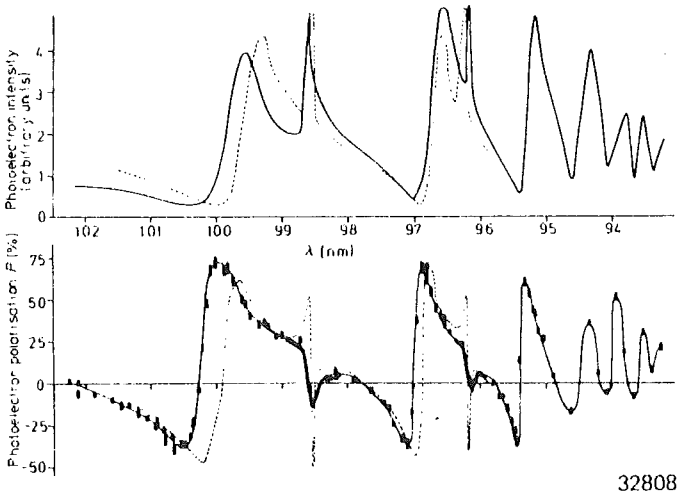


Fig. 15

Photoionisation of Xe in the autoionisation range. Upper part: cross-section, photoelectron intensity; Lower part: total spin polarisation of photoelectrons. Experimental results (——) (Ref. 46); theory (- - -) (Ref. 48). From Ref. 46).

1. C. Kunz, Synchrotron Radiation Techniques and Application, p.1, ed. C. Kunz, Topics in Current Physics, Vol. 10, Springer Verlag, Berlin Heidelberg New York (1979).
2. H. Winick, Synchrotron Radiation Research, ed. H. Winick and S. Doniach, Plenum Press, New York and London (1980).
3. U. Fano and J.W. Cooper, Rev. Mod. Physics, 40, 441 (1968).
4. A.F. Starace, Handbuch der Physik, Vol. 31, ed. W. Mehlhorn, Springer Verlag, Berlin, to be published.
5. F. Herman and S, Skillman, Atomic Structure Calculations, Prentic-Hall, Englewood Cliffs, N.J. (1963).
6. R. Haensel, G. Keitel, P. Schreiber and C. Kunz, Phys. Rev., 188, 1375 (1969).
7. J.B. West and J. Morton, Daresbury Report, DL/SRF/P130 (1978).
8. A.F. Starace, Phys. Rev. A2, 118 (1970).
9. D.J. Kennedy and S.T. Manson, Phys. Rev. A5, 227 (1972).
10. M. Ya. Amusia and N.A. Cherepkov, Case Studies in Atomic Physics, 5, 47 (1975).
11. J.A.R. Samson, Handbuch der Physik, Vol. 31, ed. W. Mehlhorn, Springer Verlag Berlin, to be published.
12. J.R. Swanson and L. Armstrong, Jr., Phys. Rev. A15, 661 (1977).
13. T.N. Chang, Phys. Rev. A15, 2392 (1977).
14. H.P. Kelly, Photoionization and other Probes of many-electron Interactions, p. 83, ed. F.J. Wuilleumier, Plenum Publishing Corporation, New York (1976).
15. H.P. Kelly, Comput. Phys. Commun. 17, 99 (1979).
16. P.G. Burke and K.T. Taylor, J. Phys. B8, 2620 (1975).
17. A. Zangwill and P. Soven, Phys. Rev. A 21, 1561 (1980.
18. A.F. Starace, Applied Optics 19, 4051 (1980).
19. J.P. Connerade, Contemporary Physics 19, 415 (1978).
20. R. Bruhn, B. Sonntag and H.W. Wolff, J.Phys. B12, 203 (1979).
21. R. Bruhn, B. Sonntag and H.W. Wolff, Phys. Lett. 69A, 9 (1978).
22. B. Sonntag, R. Haensel and C. Kunz, Solid State Commun. 7, 597 (1969).
23. J.P. Connerade, M.W.D. Mansfield and M.A.P. Martin, Proc. Roy. Soc. London A 350, 405 (1976).
24. L.C. Davis and L.A. Feldkamp, Phys. Rev. A17, 2012 (1978).
25. R. Bruhn, E. Schmidt, H. Schröder and B. Sonntag, to be published.
26. L.C. Davis and L.A. Feldkamp, Phys. Rev, to be published.
27. J. Barth, R. Bruhn, B. Sonntag and J. Weaver, Phys. Lett. 78A, 331 (1980).
28. D.L. Ederer, B.E. Cole and J.B. West, Nuclear Instr. and Methods, 172, 185 (1980).
29. A.C. Parr, R. Stockbauer, B.E. Cole, D.L. Ederer, J.L. Dehmer and J.B. West, Nuclear Instr. and Methods, 172, 357 (1980).
30. S.P. Shannon and K. Codling, J. Phys. B11, 1193 (1978).
31. D. Chandesris, C. Guillot, G. Chauvin, J. Lecante and Y. Petroff, to be published.
32. J.A.R. Samson and J.L. Gardner, Phys. Rev. Lett. 33, 671 (1974).
33. J.B. West, P.R. Woodruff, K. Codling and R.G. Houlgate, J. Phys. B9, 407 (1976).
34. M.Y. Adam, F. Wuilleumier, N. Sandner, S. Krummacher, V. Schmidt and W. Mehlhorn, Jap. J. Appl. Phys. 17-2, 170 (1978).
35. W.R. Johnson and K.T. Cheng, Phys. Rev. A20, 978 (1979).
36. T.E.H. Walker and J.T. Waber, J. Phys. B7, 674 (1974).
37. J.A.R. Samson, J.L. Gardner and A.F. Starace, Phys. Rev. A12, 1459 (1975).
38. F. Wuilleumier, M.Y. Adam, P. Dhez, N. Sandner, V. Schmidt and W. Mehlhorn, Phys. Rev.A16, 646 (1977).
39. W. Ong and S.T. Manson, J. Phys. B11, L163 (1978).
40. J. Cooper and Z.N. Zare, Lectures in Theoretical Physics, Vol. XI-C, p. 317, ed. S. Geltman, K.T. Mahanthappa and W.E. Brittin, Gordon Breach, New York (1969).
41. R.G. Houlgate, J.B. West, K. Codling and G.V. Marr, J. Electr. Spectr. 9, 205 (1976).
42. W.S. Watson and D.T. Stewart, J. Phys. B9, 466 (1974).
43. M. Ya. Amusia, N.A. Cherepkov and L.V. Chernyskeva, Phys. Lett. 40A, 15 (1972).
44. K.T. Taylor, J. Phys. B10, L699 (1977).
45. U. Heinzmann, J. Phys. B13, 4353-4381 (1980).
46. U. Heinzmann, F. Schäfers, K. Thimm, A. Wolcke and J. Kessler, J.Phys. B12, L679 (1979).
47. U. Heinzmann and F. Schäfers, J.Phys. B13, L415 (1980).
48. C.M. Lee, Phys. Rev. A10, 1598 (1974).
49. W.R. Johnson, K.T. Cheng, K.N. Huang, M.LeDourneuf, Phys. Rev. A22, 989 (1980).